

Precision lattice test of the gauge/gravity duality at large- N

Monte Carlo String/M-Theory Collaboration MCSMC

Evan Berkowitz^a Enrico Rinaldi^a Masanori Hanada^{b,c,d} Goro Ishiki^{e,f} Shinji Shimasaki^{g,h} Pavlos Vranas^a

^a*Nuclear and Chemical Sciences Division*

Lawrence Livermore National Laboratory, Livermore CA 94550, USA

^b*Stanford Institute for Theoretical Physics*

Stanford University, Stanford, CA 94305, USA

^c*Yukawa Institute for Theoretical Physics*

Kyoto University, Kitashirakawa Oiwakecho, Sakyo-ku, Kyoto 606-8502, Japan

^d*The Hakubi Center for Advanced Research*

Kyoto University, Yoshida Ushinomiyacho, Sakyo-ku, Kyoto 606-8501, Japan

^e*Center for Integrated Research in Fundamental Science and Engineering (CiRfSE)*

University of Tsukuba, Tsukuba, Ibaraki 305-8571, Japan

^f*Graduate School of Pure and Applied Sciences*

University of Tsukuba, Tsukuba, Ibaraki 305-8571, Japan

^g*Research and Education Center for Natural Sciences*

Keio University, Yokohama, Kanagawa 223-8521, Japan

^h*KEK Theory Center, High Energy Accelerator Research Organization*

Tsukuba 305-0801, Japan

E-mail: berkowitz2@llnl.gov, rinaldi2@llnl.gov,
hanada@yukawa.kyoto-u.ac.jp, ishiki@het.ph.tsukuba.ac.jp,
shinji.shimasaki@keio.jp, vranas2@llnl.gov

ABSTRACT: We pioneer a systematic, large-scale lattice simulation of D0-brane quantum mechanics. The large- N and continuum limits of the gauge theory are taken for the first time at various temperatures $0.4 \leq T \leq 1.0$. As a way to directly test the gauge/gravity duality conjecture we compute the internal energy of the black hole directly from the gauge theory and reproduce the coefficient of the supergravity result $E/N^2 = 7.41T^{14/5}$. This is the first confirmation of the supergravity prediction for the internal energy of a black hole at finite temperature coming directly from the dual gauge theory. We also constrain stringy corrections to the internal energy.

Contents

1	Introduction	1
2	D0-brane Quantum Mechanics	2
3	Lattice Setup	4
3.1	Discretized Action and Simulations	4
3.2	Observables	6
3.3	Phase Quenching	6
4	Results	8
4.1	Statistical Requirements	8
4.2	Continuum Extrapolation at Fixed N	10
4.3	Simultaneous Large N and Continuum Extrapolation	11
5	Supergravity and Black Hole Internal Energy	13
5.1	SUGRA at Low Temperatures	14
5.2	Subleading Temperature Dependence	16
5.3	$\mathcal{O}(N^{-2})$ Corrections	17
6	Discussion	18
	Acknowledgements	19
	References	20
A	Correlations Between Polyakov Loop and Internal Energy	22
B	Lattice Measurements	24
C	Simultaneous Continuum Large-N Extrapolations	28

1 Introduction

The gauge/gravity duality conjecture claims that superstring theories and certain supersymmetric gauge theories are equivalent [1–3]. This duality implies that gauge theories provide us with a non-perturbative formulation of superstring theories, which will be essential in understanding the nature of quantum gravity. However, this duality between gauge theories and gravity is still a conjecture. With the aim to establish a non-perturbative formulation of superstring theories based on the duality relation, we must vigorously try to falsify the duality.

Gauge/gravity duality can be intuitively understood as a relation between two different descriptions of a system with some D-branes in a string theory. One description of D-branes

is given by the low energy effective theory of open strings, where the D-branes are described by a supersymmetric Yang-Mills theory defined on the world-volume of the D-branes. On the other hand, D-branes can also be thought of as solitonic objects in theories of closed strings, which couple to gravity in the bulk. In this picture, the D-branes are described as a source of gravity. This leads to another description of the D-branes in terms of the bulk gravitational theory.

Though the equivalence between these two descriptions is naturally expected from the physical viewpoint, no rigorous proof has been given so far. A major obstacle is the fact that, in the duality, the perturbative semi-classical regime of superstring theory is mapped to the non-perturbative regime of the gauge theory, which is very hard to deal with in an analytical way. In order to study the duality, one needs a method of analyzing supersymmetric gauge theories in the strong coupling regime.

Numerical simulations of gauge theories, based on lattice discretization, for example, are a powerful tool to study such a regime. By using a discretized lattice theory, one has a robust framework to work with in order to extract information about non-perturbative physics. This is what makes it possible to test the gauge/gravity duality from first principles.

For the duality based on D0-branes a lot of positive evidence has been obtained through numerical simulations of a supersymmetric gauge theory known as D0-brane quantum mechanics. In this case, the gravity dual geometry is given by the black 0-brane solution in type IIA supergravity (SUGRA) [4]. At finite temperature, the black 0-brane is characterized by thermodynamic quantities such as entropy and internal energy. In particular, at large- N and low temperature, where the SUGRA approximation becomes valid, the internal energy is given by

$$E = 7.41N^2T^{14/5}, \quad (1.1)$$

where, E and T are dimensionless internal energy and temperature normalized by appropriate powers of the 't Hooft coupling of D0-brane quantum mechanics.

In this paper, we test the duality for D0-branes by performing a systematic, large-scale lattice study of D0-brane quantum mechanics. In particular, we take both the continuum limit, by sending the lattice spacing to zero, and the large- N limit for the first time. This makes possible precise comparison with the result (1.1) in the SUGRA approximation. We calculate the internal energy of D0-brane quantum mechanics and confirm that the internal energy of the black 0-brane (1.1) is reproduced from the D0-brane quantum mechanics — our value is $E = (7.4 \pm 0.5)N^2T^{14/5}$. We also give predictions for the stringy corrections directly from the gauge theory side.

The rest of this paper is organized as follows. In Section 2, we review D0-brane quantum mechanics in more details and describe the existing literature. Section 3 contains the setup of our lattice simulations and the observables used to test the gauge/gravity duality. In Section 4 we discuss our lattice results and their extrapolation to the continuum and large- N limits, before comparing them to the SUGRA expectations in Section 5.

2 D0-brane Quantum Mechanics

We consider D0-brane quantum mechanics [5], which is the low energy effective theory of open strings ending on N D0-branes in 10-dimensional flat space. The Lagrangian in the

Euclidean signature is

$$\mathcal{L} = \frac{1}{g_{YM}^2} \text{Tr} \left\{ \frac{1}{2} (D_t X_M)^2 - \frac{1}{4} [X_M, X_{M'}]^2 + i \bar{\psi}^\alpha D_t \psi^\beta + \bar{\psi}^\alpha \gamma_{\alpha\beta}^M [X_M, \psi^\beta] \right\}. \quad (2.1)$$

Here, X_M ($M = 1, 2, \dots, 9$) and ψ_α ($\alpha = 1, 2, \dots, 16$) are $N \times N$ bosonic and fermionic Hermitian matrices, the covariant derivative D_t is given by $D_t = \partial_t + i[A_t, \cdot]$ where A_t is the $U(N)$ gauge field, and $\gamma_{\alpha\beta}^M$ are the left-handed part of the gamma matrices in (9+1)-dimensions, which are 16×16 matrices. This action can be obtained by dimensionally reducing the $\mathcal{N} = 1$ 10D super Yang–Mills or $\mathcal{N} = 4$ 4D SYM to (0 + 1)-dimension.

Historically, this model was also obtained by applying the matrix regularization to the theory of a single supermembrane in 11-dimensional flat space in the light-cone frame [6]. From this perspective, it was conjectured that the model in Equation 2.1 describes second quantized M-theory on 11-dimensional flat space [5]. The coupling constant g_{YM} and the matrix size N are related to parameters of the M-theory as $g_{YM}^2 N \sim R^3$ and $N \sim p^+ R$, where R is the radius of the M-circle and p^+ is momentum along the light-cone direction. In order to realize the decompactified limit $R \rightarrow \infty$ with p^+ fixed, one needs to take a very strong coupling limit of the matrix model.

On the other hand, in this paper, we mainly consider the 't Hooft limit of the model, where $\lambda = g_{YM}^2 N$ is fixed and $N \rightarrow \infty$. Therefore we focus on the gauge/gravity duality to type IIA superstring theory [4]. The coupling constant λ has mass dimension 3 and sets the scale of the theory. In the following we fix $\lambda = 1$ without loss of generality, because it amounts to a rescaling of the fields.

Intuitively, the off-diagonal elements of the matrices are open strings that connect the D0-branes whose locations are given by the diagonal elements [7], as sketched in Fig. 1. Black 0-branes are states where all the D0-branes form a single bound bunch, which corresponds to generic non-commuting matrices. Strictly speaking, such bound state and a black 0-brane in SUGRA can be equivalent only at large- N and in the strong coupling limit (low temperature¹). However the bound state at generic N and temperature is connected smoothly to the black 0-brane at large- N and strong coupling. Hence it can be regarded as the stringy generalization of the black hole. When there is no risk of confusion, we call such bound state simply as the black 0-brane or black hole.

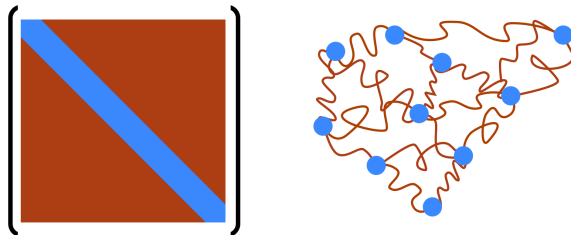


Figure 1. An intuitive interpretation of the matrices X_M . The diagonal elements correspond to positions of D0-branes and the off-diagonal elements correspond to the open strings connecting them. This figure is taken from Ref. [8].

¹Low temperature means that the temperature T is much smaller than the typical energy scale, $\lambda^{1/3}$. Hence this implies a strong coupling $\lambda^{-1/3} T \ll 1$.

D0-brane quantum mechanics was first investigated with Monte Carlo methods in Ref. [9]. (Earlier numerical work with the same motivation can be found in Ref. [10].) Previously, there have been attempts to study the internal energy [9, 11–14], the supersymmetric Polyakov loop [15] and two-point correlation functions [16, 17].

However, the existing literature claiming to provide strong evidence supporting the gauge/gravity duality could be invalidated, because the numerical results obtained so far were not extrapolated to the continuum limit $L \rightarrow \infty$ and the $N \rightarrow \infty$ limit. This lack of controlled extrapolations would obstruct a meaningful test of the conjecture. Moreover, the existing results did not have enough accuracy to confirm the supergravity prediction of the internal energy, $E/N^2 = 7.41T^{14/5}$. In order to achieve high precision, it is of paramount importance to correctly estimate the discretization errors and corrections due to finite N . We accomplish this for the first time in our study.

3 Lattice Setup

In order to study the thermodynamic properties the D0-brane quantum mechanics non-perturbatively, we discretize the theory in a 0+1 dimensional Euclidean spacetime. We then use the discretized action to calculate the theory's partition function by importance sampling field configurations via the rational hybrid Monte Carlo algorithm. By measuring observables on this ensemble of configurations, we get an estimate for the observable's expectation value with an associated statistical uncertainty. Finally, by measuring on ensembles with different lattice spacings, we can extrapolate to the continuum limit, removing the lattice regulator, and get a fully non-perturbative result. As we will show, achieving a reliable continuum extrapolation requires a careful study.

3.1 Discretized Action and Simulations

Consider D0-brane quantum mechanics (2.1) on a Euclidean circle with circumference β . With antiperiodic boundary conditions for the fermions and periodic boundary conditions for the bosons, β is identified with the inverse temperature $1/T$.

This model consists of nine $N \times N$ bosonic hermitian matrices X_M ($M = 1, 2, \dots, 9$), sixteen fermionic matrices ψ_α ($\alpha = 1, 2, \dots, 16$) and the gauge field A_t . Both X_M and ψ_α are in the adjoint representation of $U(N)$ gauge group, and the covariant derivative D_t acts on them as $D_t X_M = \partial_t X_M + i[A_t, X_M]$ and $D_t \psi_\alpha = \partial_t \psi_\alpha + i[A_t, \psi_\alpha]$. The 't Hooft coupling $\lambda = g_{YM}^2 N$ has a dimension of (mass)³, and can be set to 1 by rescaling time t and the fields. In other words, all dimensionful quantities can be made dimensionless by multiplying appropriate powers of λ . As mentioned before, we choose $\lambda = 1$. The action is given by

$$S_{BFSS} = S_b + S_f, \quad (3.1)$$

where S_b the bosonic part and S_f the fermionic part are given by

$$S_b = N \int_0^\beta dt \operatorname{Tr} \left\{ \frac{1}{2} (D_t X_M)^2 - \frac{1}{4} [X_M, X_N]^2 \right\}, \quad (3.2)$$

$$S_f = N \int_0^\beta dt \operatorname{Tr} \{ i \bar{\psi} \gamma^{10} D_t \psi - \bar{\psi} \gamma^M [X_M, \psi] \}. \quad (3.3)$$

while γ^M ($M = 1, \dots, 10$) represent the 16×16 left-handed part of the 10D gamma matrices Γ^M . Formally, this model is obtained by dimensionally reducing the ten-dimensional $\mathcal{N} = 1$ super Yang-Mills theory to one dimension. The index α of the fermionic matrices ψ_α corresponds to the spinor index in ten dimensions, and ψ_α is Majorana-Weyl in the ten-dimensional sense.

For numerical efficiency, we adopt the static diagonal gauge [18],

$$A_t = \frac{1}{\beta} \cdot \text{diag}(\alpha_1, \dots, \alpha_N), \quad -\pi < \alpha_i \leq \pi. \quad (3.4)$$

Associated with this gauge fixing, we add to the action the corresponding Faddeev-Popov term

$$S_{F.P.} = - \sum_{i < j}^N 2 \log \left| \sin \left(\frac{\alpha_i - \alpha_j}{2} \right) \right|. \quad (3.5)$$

We regularize the theory by discretizing the Euclidean time direction over L lattice sites. Our lattice action is

$$S_b = \frac{N}{2a} \sum_{t,M} \text{Tr} \left\{ (D_+ X_M(t))^2 \right\} - \frac{Na}{4} \sum_{t,M,N} \text{Tr} \left\{ [X_M(t), X_N(t)]^2 \right\}, \quad (3.6)$$

$$S_f = \sum_t \text{Tr} \left\{ iN \bar{\psi}(t) \begin{pmatrix} 0 & D_+ \\ D_- & 0 \end{pmatrix} \psi(t) - aN \sum_{t,M} \bar{\psi}(t) \gamma^M [X_M(t), \psi(t)] \right\}, \quad (3.7)$$

$$S_{F.P.} = - \sum_{i < j}^N 2 \log \left| \sin \left(\frac{\alpha_i - \alpha_j}{2} \right) \right|, \quad (3.8)$$

where the gauge links $U = \exp(iaA_t)$ with $-\pi \leq \alpha_i < \pi$. The covariant derivative D_\pm can be discretized in different ways which in turn will have different discretization errors. A first discretization that we call “unimproved” defines D_\pm as follows:

$$\begin{aligned} D_+ f(t) &= U f(t+a) U^\dagger - f(t), \\ D_- f(t) &= f(t) - U^\dagger f(t-a) U, \end{aligned} \quad (3.9)$$

where $f(t)$ can be a bosonic or a fermionic field defined at site t and the gauge link U is t -independent due to our gauge fixing choice (3.4). This discretized derivative is related to the continuum one D_t by $D_\pm f(t) = a D_t f(t) + \mathcal{O}(a^2)$. The discretization of D_\pm that we will use in our main results has smaller discretization effects, $\mathcal{O}(a^3)$, and we call it “improved” to reflect this feature. The exact lattice definition is

$$\begin{aligned} D_+ f(t) &= -\frac{1}{2} U^2 f(t+2a) U^{\dagger 2} + 2U f(t+a) U^\dagger - \frac{3}{2} f(t), \\ D_- f(t) &= +\frac{1}{2} U^{\dagger 2} f(t-2a) U^2 - 2U^\dagger f(t-a) U + \frac{3}{2} f(t). \end{aligned} \quad (3.10)$$

We calculate with the unimproved and improved lattice actions with the RHMC algorithm, tuning the integration step and trajectory length to attain an acceptance rate of order 80%. We take advantage of MPI parallelization, where each MPI process takes care l lattice sites and $n \times n$ sub-blocks of matrices. The number of total processes for a lattice

of size L and matrices of size $N \times N$ is $(L/l) \cdot (N/n)^2$. Typically we take $n = l = 4$ and, for example, the number of processes is $8^3 = 512$ for $N = L = 32$. This setup is very advantageous on large parallel machines and allows us to simulate very large values of N and L by scaling our code to greater numbers of MPI processes. The simulation code is publicly available and well documented [19].

An important remark for numerical simulations of the D0-brane quantum mechanics is that the system has flat directions, $[X_M, X_{M'}] = 0$. At large N , the flat directions are lifted dynamically, around the black hole phase. However, at finite N , the black hole is metastable, and the D0-branes (the eigenvalues of the matrices) can be emitted and propagate to infinity. This phenomenon produces an instability in the Monte Carlo evolution which become more and more severe at smaller N and at lower temperatures. In order to obtain meaningful statistical results from simulations, it is of crucial importance to control these flat directions and correctly single out the phase under consideration [9, 20, 21]. If this control is missing, wrong answers might be obtained, as happened countless many times in the early literature on lattice supersymmetry. In this study, we overcome the instability by taking N sufficiently large that our observables do not show signs of eigenvalue instability over long Monte Carlo histories.

3.2 Observables

On each configuration we measure different observables. The most crucial for this work is the internal energy E/N^2 ,

$$E/N^2 = \frac{3}{2N^2\beta} (9(N^2L - 1) - 2\langle S_b \rangle). \quad (3.11)$$

We also measure the absolute value of the Polyakov loop,

$$|P| = \left| \frac{1}{N} \sum_{j=1}^N e^{i\alpha_j} \right| \quad (3.12)$$

where α_j belong to the gauge-fixed link variables, the average size of the eigenvalue bunch (0-brane) R^2 ,

$$R^2 \equiv \frac{1}{NL} \sum_{M,t} \text{Tr} \{ X_M^2 \} \quad \longrightarrow \quad \frac{1}{N\beta} \int dt \text{Tr} X_M^2 \quad (3.13)$$

and the potential term F^2 (analogous to the square of the field strength),

$$F^2 = -\frac{1}{NL} \sum_{M,M',t} \text{Tr} \{ [X_M, X_{M'}]^2 \} \quad \longrightarrow \quad -\frac{1}{N\beta} \int dt \text{Tr} [X_M, X_{M'}]^2. \quad (3.14)$$

3.3 Phase Quenching

One potential issue in simulating this theory is the infamous sign problem — the Pfaffian that results from integrating out the fermions can have an oscillating phase, undermining the probabilistic interpretation of the Euclidean action in the path integral. In our calculation, we follow the usual practice [9, 11–14] of simply taking the absolute value of the Pfaffian, quenching the phase.

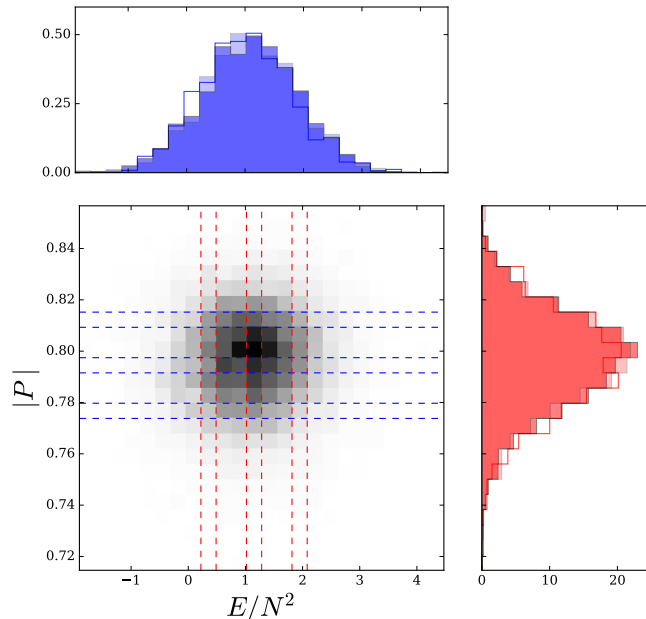


Figure 2. The correlation between E/N^2 and $|P|$ at $N = 16$, $L = 16$ and $T = 0.5$ is shown as 2D histogram where a darker color corresponds to a higher count. The blue and red histograms (three per panel) represent the normalized distribution of E/N^2 and $|P|$, respectively, within the slices on the two-dimensional plot bounded by dashed lines. The histograms coming from different slices are almost indistinguishable.

Several studies have found that the phase of the Pfaffian remains close to zero in the temperature region we consider, and the most recent one is Ref. [14]. This means that the sign problem is mild and quenching the phase does not distort the results. Previous results were obtained for relatively small values of N and of the cutoff, but in the same temperature regime we study here.

In principle, the effect of the phase can be taken into account by phase reweighting,

$$\langle \mathcal{O} \rangle_{\text{F}} = \frac{\langle \mathcal{O} \cdot e^{i\theta} \rangle_{\text{PQ}}}{\langle e^{i\theta} \rangle_{\text{PQ}}}, \quad (3.15)$$

where $\langle \cdot \rangle_{\text{F}}$ and $\langle \cdot \rangle_{\text{PQ}}$ represent the expectation values with the full and phase-quenched theories, and $e^{i\theta} = \text{Pfaffian}/|\text{Pfaffian}|$. Interestingly, even when the phase fluctuations become large, it has been observed that the phase quenching does not affect the expectation values of various observables.

A possible mechanism is suggested in Ref. [17]. Let $\rho(x)$ be the distribution of the observable \mathcal{O} in the phase-quenched simulation, and let w_x be the average of $e^{i\theta}$ when the value of \mathcal{O} is fixed to x . Then

$$\langle \mathcal{O} \rangle_{\text{PQ}} = \int dx x \rho(x) \quad (3.16)$$

$$\langle \mathcal{O} \cdot e^{i\theta} \rangle_{\text{PQ}} = \int dx x \rho(x) w_x \quad (3.17)$$

$$\langle e^{i\theta} \rangle_{\text{PQ}} = \int dx \rho(x) w_x . \quad (3.18)$$

Typically $\rho(x)$ peaks around the average value, $x = \langle \mathcal{O} \rangle_{\text{PQ}}$. If w_x is constant around this peak, then $\langle \mathcal{O} \cdot e^{i\theta} \rangle_{\text{PQ}} \simeq \langle \mathcal{O} \rangle_{\text{PQ}} \cdot \langle e^{i\theta} \rangle_{\text{PQ}}$, and then (3.15) becomes $\langle \mathcal{O} \rangle_{\text{F}} \simeq \langle \mathcal{O} \rangle_{\text{PQ}}$.

Because the calculation of the Pfaffian is very costly, it is difficult to test this scenario directly at large values of N . However, it is possible to indirectly infer the magnitude of the phase fluctuations and their impact on the other observables. In fact, the Polyakov loop has a strong correlation with the phase factor—the phase disappears when $|P| = 1$ (up to discretization effects) and the phase fluctuations become larger as $|P|$ decreases. In Fig. 2, we show the correlation between E/N^2 and $|P|$ at $N = 16$, $L = 16$ and $T = 0.5$. The blue and red histograms represent the distribution of E/N^2 and $|P|$, respectively, with the other quantity restricted within small bins highlighted in the two-dimensional plot. The areas of the histograms are normalized. The E -independence of the distribution of $|P|$, at least away from the tails, strongly suggests the E -independence of the distribution of the phase, which justifies the phase quenching via the scenario explained above. A more detailed study of the distribution of $|P|$ for various values of the energy, near and away from its average, is reported in Appendix A.

An explicit calculation of the Pfaffian phase is worthwhile, but we leave it for a future study. In the rest of the paper we assume that the phase-quenched approximation does not influence the internal energy results of our simulations.

4 Results

In this section we discuss the statistical needs of our analysis, continuum extrapolations at fixed N (comparing with other calculations when available) and simultaneous continuum and large- N extrapolations. In the end we report a continuum large- N data set that we will use in Section 5 for a direct comparison to supergravity predictions. We also collect our measurements for each ensemble in Appendix B.

4.1 Statistical Requirements

To ensure a faithful estimation of an observable, one must ensure a large number of independent (decorrelated) Monte Carlo samples are taken. In Fig. 3 we show an example Monte Carlo history for the ensemble with $N = 24$, $L = 32$, and $T = 0.5$. It is apparent that there are long-lived autocorrelations. Therefore, to achieve many independent samples, lengthy Monte Carlo ensembles are required.

Moreover, accounting for autocorrelations is essential for an accurate estimate of the statistical uncertainty on a given measurement. For each observable on each ensemble, we measure the autocorrelation time τ_{corr} using the Madras-Sokal algorithm and form bins of width $3\tau_{\text{corr}}$. With those binned measurements we perform a jackknife analysis to estimate the statistical uncertainty. We also independently test that the statistical error associated with our final average is robust by performing different analysis with smaller and larger jackknife bins and making sure that the final uncertainty does not change.

In Fig. 4 we study the statistical stability of E/N^2 for a low-temperature ensemble, $N = 24$, $L = 32$, and $T = 0.5$, with bins 50 trajectories wide. In the left panel we show the residual effects of keeping measurements from too early in the Monte Carlo history by using

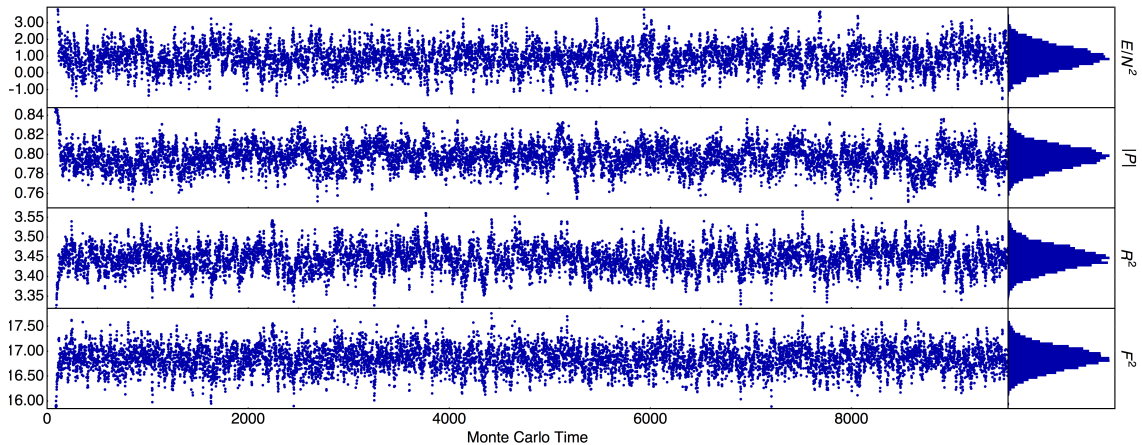


Figure 3. The Monte Carlo history and a corresponding histogram for the energy E/N^2 , the Polyakov loop $|P|$, R^2 , and F^2 of the $T = 0.5$ $N = 24$ $L = 32$ ensemble. For each observable, one can see fluctuations that span many Monte Carlo steps.

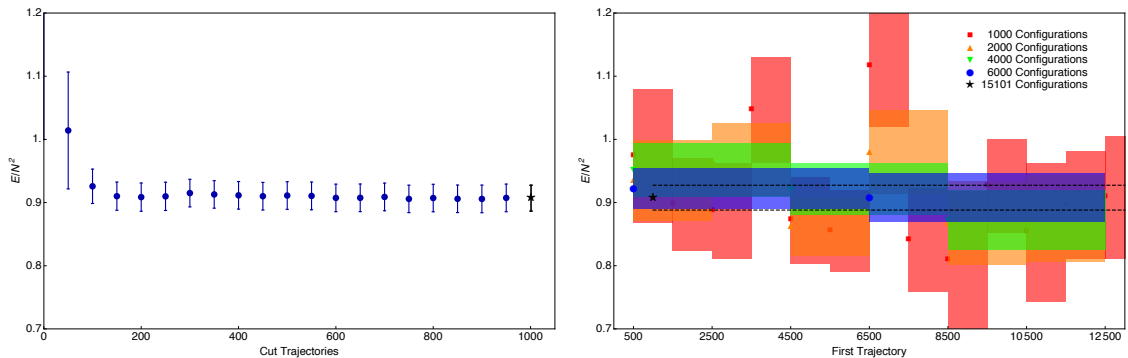


Figure 4. A study of the statistical stability of E/N^2 for the ensemble $N = 16$, $L = 32$, $T = 0.5$. In the left panel we show different thermalization cuts, measuring E/N^2 on the rest of the configurations. In the right panel we show the importance of large statistical samples by measuring on consecutive disjoint sets of trajectories. As the statistical sample grows from 1000 configurations (red squares) to 6000 configurations (blue circles), the central values and uncertainties between sets of configurations become more and more stable and compatible. In both panels we perform the analysis with bins of 50 configurations. For comparison, we also show our final analysis and its uncertainty as a black star in both panels, with its error bar displayed as dashed lines on the right panel.

the whole ensemble and only adjusting the thermalization cut. From the compatibility with later cuts, it is clear that this ensemble has no memory of its initially chosen configuration after 500 trajectories. On each ensemble, we discard 1000 trajectories as a thermalization cut.

In the right panel of Fig. 4 we show how many configurations are necessary for a stable estimate. We start at trajectory 500 and take the next 1000, 2000, 4000, and 6000 trajectories and perform an independent analysis, and then slide that window to the next disjoint set of trajectories. One can see that for this ensemble, 1000 thermalized trajectories is not enough to achieve a stable statistical estimate, indicating that there can be sizable fluctua-

tions over Monte Carlo time that can dramatically shift the measured value. However, 2000 trajectories seem to be enough to reliably get the eventual central value within the uncertainty. Increasing the window size correctly washes out the effect of lengthy fluctuations and makes each successive analysis agree more reliably. We are therefore confident that most of our statistical samples are large enough to correctly estimate the energy E/N^2 .

Some ensembles at $T = 0.4$ are not very lengthy—though all are longer than 1000 trajectories after the thermalization cut. To compensate for this shortcoming, we inflated their statistical uncertainty by 50% and reperformed all the following analyses. We find very little difference between the two cases. In what follows, we therefore use the uninflated errors.

4.2 Continuum Extrapolation at Fixed N

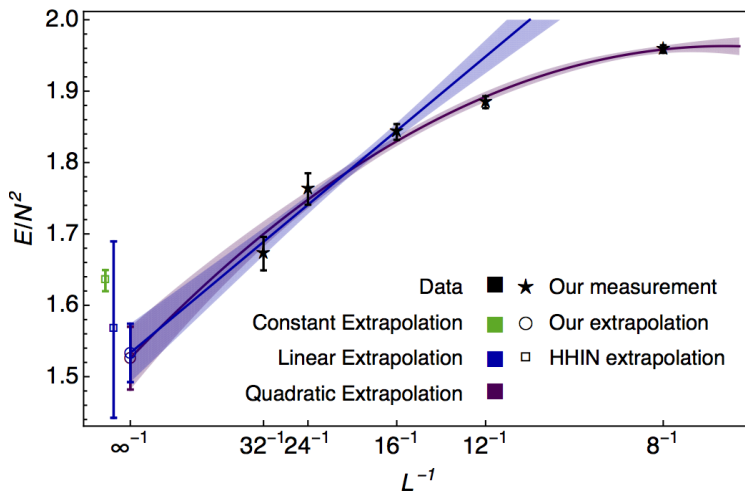


Figure 5. A continuum extrapolation for $T = 0.7$ with fixed $N = 16$ with the improved action. Black stars represent our measurements, open circles our extrapolation, and open squares the extrapolation from Ref. [20]. Error bars and the error bands on the extrapolated curves represent 1σ errors. Our linear extrapolation is only fit to the data at $L \geq 16$. The divergence of the linear and quadratic extrapolations indicate that for this ensemble, linear extrapolations of lattice data that include data taken at $L \lesssim 16$ will be systematically biased.

To study the continuum theory, one must measure at a variety of lattice discretizations and extrapolate to the continuum. In this section, we discuss continuum extrapolation at fixed N using our unimproved and improved actions (cfr. equations (3.9) and (3.10)).

As the lattice spacing L^{-1} gets smaller, one expects an expansion around $L^{-1} = 0$ to get better. So, at fixed N the energy should follow

$$\frac{E}{N^2} = e_0 + \frac{e_1}{L} + \frac{e_2}{L^2} + \mathcal{O}(L^{-3}) \quad (4.1)$$

where e_0 is the continuum-extrapolated value and the other e_i characterize the lattice artifacts. Based on the naïve scaling of the action with the lattice spacing, we expect results with the unimproved action to have larger discretization effects and we check this explicitly in the following for the first time.

In Figure 5 we show a fixed- N continuum extrapolation for $T = 0.7$ $N = 16$ so that we can directly compare to the continuum extrapolations of Ref. [20]. One immediately sees that the region where only the leading L^{-1} corrections matter is $L \gtrsim 16$ —with smaller L the subleading correction is not negligible, so linear fits to lattice data from such small L will be systematically biased towards larger E/N^2 . We have checked this rule of thumb for all T and N , and find broad consistency with this observation, which means Refs. [14, 20] may suffer from premature extrapolation.

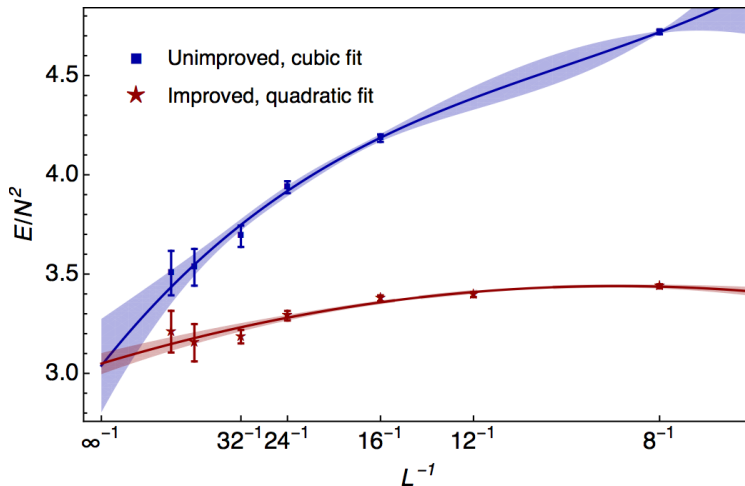


Figure 6. A comparison between taking the continuum limit for the unimproved and improved actions for $T = 1.0$, $N = 16$. Error bars and the error bands on the extrapolated curves represent 1σ errors.

Knowing that to successfully fit down to $L = 8$ with the improved action requires a quadratic fit, we expect additional lattice artifacts to contaminate $L = 8$ with the unimproved action, suggesting an additional term is needed to fit the unimproved action to incorporate that point into the continuum limit. Indeed, fitting a quadratic to that point pushes the fit upwards, while fitting a cubic gives perfect agreement with the improved continuum limit. Using the improved action allows us to extrapolate to the continuum in a more controlled manner, because a successful extrapolation requires fitting fewer parameters.

4.3 Simultaneous Large N and Continuum Extrapolation

In order to test the gauge/gravity duality precisely, it is important to take the large- N limit. However, taking the continuum limit at large- N becomes costly even with a quadratic fit, because at small N the physical instability may ruin the Monte Carlo history, while numerical cost grows with L and N .

Large- N corrections appear in powers of N^{-2} , at each fixed L , because the 't Hooft counting holds even for the discretized theory. Thus, at a fixed temperature we expect E/N^2 to be described by a series like the following

$$\frac{E}{N^2} = \sum_{i,j \geq 0} \frac{e_{ij}}{N^{2i} L^j} \quad (4.2)$$

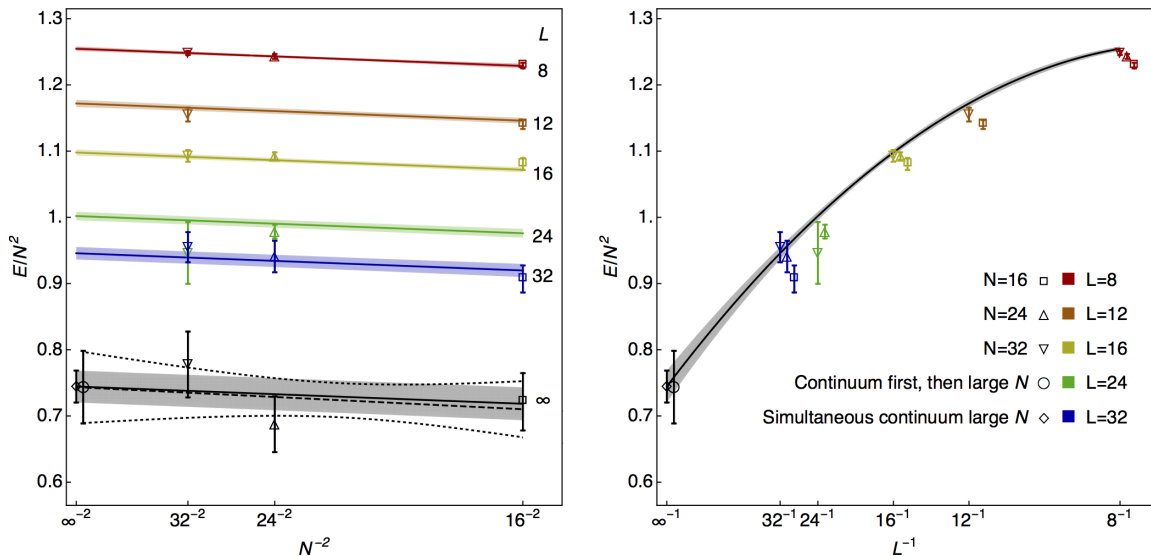


Figure 7. A simultaneous continuum- and large- N extrapolation for $T = 0.5$ with the improved action. All the data points are fit to a single 2D surface given by (4.3). In the right panel, we show all the data points (slightly offset for visual clarity) and the (black) $N = \infty$ slice of the fitted surface. In the left panel, we show all the data points and the (black) continuum extrapolations at each N together with their subsequent large- N limit as the dashed line with uncertainties given by the dotted band. We also show the fixed- L slices of the 2D fit, as well as the (black) $L = \infty$ slice. In both panels, the black circle represents the result of taking the large- N limit of the continuum extrapolations at each N , while the best-fit simultaneous continuum- and large- N limit e_{00} is shown as a black diamond. Error bars, the error band on the extrapolated surface, and the dotted error band represent 1σ uncertainties.

so that e_{i0} are physical, continuum-limit quantities at finite N , e_{00} is the continuum, large- N value, and all other coefficients, e_{ij} with $j > 0$, characterize lattice artifacts. Importantly, by extrapolating in $1/N^2$ and $1/L$ simultaneously, we can take advantage of significantly more data points without increasing the number of fit parameters dramatically.

We can truncate (4.2) in various ways and attempt to fit a finite set of e_{ij} . We attempted a six-parameter fit with $i + j \leq 2$ and found our data insufficient to characterize e_{11} or e_{20} without 100% uncertainties, and strong correlation with the other coefficients. We also performed five-parameter fits, omitting either e_{11} and e_{20} and still found the other to be very poorly constrained by our data and highly correlated with the remaining coefficients. Thus, we settled on a four-parameter fit—next to leading order (NLO) in N^{-2} and NNLO in L^{-1} , with no mixed term

$$\frac{E}{N^2} \approx e_{00} + \frac{e_{01}}{L} + \frac{e_{02}}{L^2} + \frac{e_{10}}{N^2}. \quad (4.3)$$

We fit this form to all of our measurements at a given temperature, and find extremely good fit quality together with a very mild dependence on N and—just as in the fixed- N case—important dependence on L .

The strong L dependence, which we observe to get stronger at low temperature, raises the possibility that Ref. [12], which at low temperature works only at $L = 16$ and has

no continuum limit, and Ref. [20], which at $N = 16$ extrapolates from the momentum cutoff $\Lambda \leq 8$, may be systematically contaminated by discretization artifacts. However, because those references use different discretized actions from that used in this work, their discretization effects may be substantially smaller than in our approach. For example, a direct comparison at $T = 0.4$ $N = 32$ $L = 16$ shows that Ref. [12]’s central value is substantially closer to our continuum limit 0.40(7) than our data point at those parameters 0.835(7).

In Figure 7 we show the result of the simultaneous continuum- and large- N extrapolation of the measurements of the $T = 0.5$ improved action measurements. We also show three fixed- N continuum extrapolations and their subsequent large- N extrapolation. For that ensemble, we fit 13 data points to the four-parameter fit in (4.3) and find a reduced chi-squared (the usual χ^2 divided by DOF, the degrees of freedom in the fit) of 7.2/9 and good compatibility with the sequential extrapolation.

In Table 1 we show the simultaneous continuum and large- N extrapolation by the four-parameter fit in (4.3) of data taken with the improved action at various temperatures. A more complete data set is provided in Appendix C.

T	e_{00}	$-e_{10}$	χ^2	DOF
0.4	0.38±0.06	5.4±9.2	1.3	4
0.5	0.74±0.02	6.7±1.5	7.2	9
0.6	1.15±0.02	5.0±1.8	8.8	8
0.7	1.54±0.03	3.9±2.0	8.8	8
0.8	1.99±0.03	6.2±2.5	15.1	8
0.9	2.57±0.04	11.9±2.9	3.3	8
1.0	3.11±0.04	8.4±3.2	8.9	10

Table 1. The continuum energy coefficients e_{00} (large- N) and e_{10} (leading $1/N^2$ correction) for different temperatures, the χ^2 of the extrapolating fit, and the degrees of freedom for that fit. In every case χ^2/DOF is between 0.3 and 1.9.

5 Supergravity and Black Hole Internal Energy

To ultimately check the gauge/gravity duality, we want to compare our gauge-theory calculations with supergravity (SUGRA) and superstring calculations. As is thoroughly reviewed in Ref. [20]², the internal energy of the black 0-brane can be expanded with respect to T and $1/N^2$ as

$$\begin{aligned} \frac{E}{N^2} &= \frac{(a_0 T^{14/5} + a_1 T^{23/5} + a_2 T^{29/5} + a_3 T^{32/5} + \dots)}{N^0} + \frac{(b_0 T^{2/5} + b_1 T^{11/5} + \dots)}{N^2} + \mathcal{O}\left(\frac{1}{N^4}\right) \\ &= \frac{E_0(T)}{N^0} + \frac{E_1(T)}{N^2} + \mathcal{O}\left(\frac{1}{N^4}\right) \end{aligned} \quad (5.1)$$

²The study of α' and g_s corrections based on string perturbation theory has a long history. In the example of the type IIA black 0-brane under consideration, the α' expansion corresponds to the expansion with $\alpha'/R_{BH}^2 \sim T^{3/5}$, where R_{BH} is the curvature radius of the black hole geometry. At tree level, it starts with $(\alpha')^3$ [22–25] and is followed by $(\alpha')^5, (\alpha')^6, \dots$ [26, 27]. A more detailed argument including g_s corrections can be found in Ref. [28], Ref. [29] and references therein.

where a_0 and b_0 are known by exact calculations to be approximately 7.41 and -5.77 respectively. We group the coefficients at a fixed order in N into the functions $E_i(T)$. On the gauge-theory side of the duality, these functions should be reproduced by our coefficients e_{i0} reported in Tab. 1.

In this section we will present a variety of fits comparing our extrapolated values in Tab. 1 to these forms and we will summarize our findings in the next section. At each temperature, we have access to the continuum large- N behavior (E_0 through e_{00}) and the $1/N^2$ correction (E_1 through e_{10}) independently. This allows us to fit the different orders of N^2 in (5.1) separately.

5.1 SUGRA at Low Temperatures

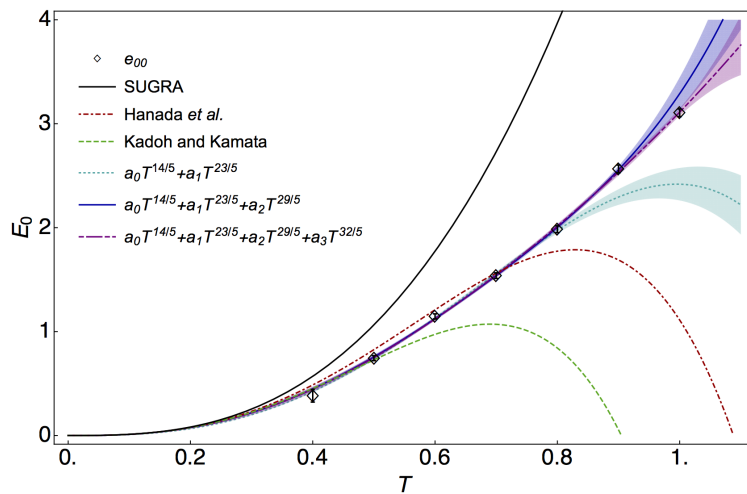


Figure 8. Our best fits of E_0 to the data points e_{00} shown as black diamonds, including the first two/three/four terms as a cyan dotted line/blue solid line/purple dot-dot-dashed line with 1σ error bands. We also show the result from Ref. [12] and Ref. [11] results as green dashed and red dot-dashed lines, respectively. The SUGRA result is shown in black.

First, let us confirm that our continuum and large- N data are consistent with the SUGRA prediction, in that they reproduce the SUGRA calculation of the leading coefficient $a_0 = 7.41$. The agreement between D0-brane quantum mechanics and SUGRA is our main result. Checking the value of a_0 against lattice simulations is a non-trivial task and is usually hindered by numerical results with large error bars or with undefined systematic errors.

We fit the $\mathcal{O}(N^0)$ coefficients, including the leading-order coefficient known from supergravity. We perform two fits of E_0 to e_{00} , fitting a_0 and a_1 , including or excluding a_2 . We exclude the $T = 1.0$ data point, because the assumption $T \ll 1$ is certainly broken there. In Fig. 8 we show the best fits of $E_0(T)$, together with previous estimates of the same function and the SUGRA result.

The fit that excludes a_2 struggles to capture the full behavior of the data, and in the best case (fitting to $T \leq 0.8$) produces $a_0 = 6.2 \pm 0.2$, substantially different from the supergravity result, and $a_1 = -3.8 \pm 0.3$. However, this can be understood as a systematic

issue—trying to capture too much temperature dependence without including the next term of E_0 distorts the coefficients. The term with the a_2 coefficient is as important as the one with a_1 and should be fitted together in the temperature region of our data. In fact, also fitting a_2 relieves the tension between the two terms and produces

$$a_0 = 7.4 \pm 0.5 \quad a_1 = -9.7 \pm 2.2 \quad a_2 = 5.6 \pm 1.8 \quad \chi^2/\text{DOF} = 2.6/3.$$

Adding an additional term a_3 representing a higher order α' -correction does not modify the above results, while the uncertainties increase dramatically.

Our value for a_0 is entirely consistent with the SUGRA-predicted value of 7.41 and has a very small uncertainty $\sim 7\%$. This agreement may be considered a *bona fide* direct test of the gauge/gravity duality: if the D0-brane quantum mechanics and supergravity results differed, we could have falsified the correspondence.

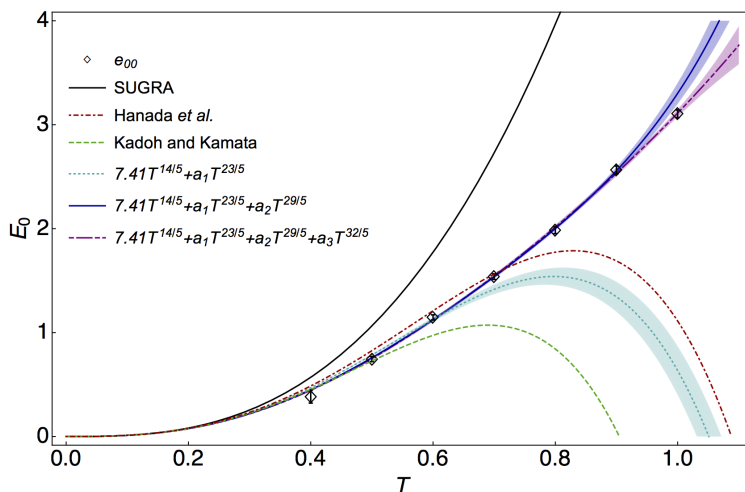


Figure 9. The same as in Fig. 8, but with a_0 fixed to its known SUGRA value, rather than fit.

We have also fit a_1 and a_2 while fixing the known SUGRA value $a_0 = 7.41$. If we exclude a_2 , we do not get a good fit, even if we change the fitting window. Including a_2 dramatically improves the fit—we can comfortably incorporate all the data up to $T < 1$. The best fit is to $T \leq 0.9$ and gives $a_1 = -10.0 \pm 0.4$ and $a_2 = 5.8 \pm 0.5$, describes the data well ($\chi^2/\text{DOF}=2.6/4$), and is in very good agreement with our best fit when we did not demand the SUGRA value $a_0 = 7.41$ —further bolstering our confidence in that result.³

The full form of E_0 in (5.1) is actually, on the gravity side, an expansion in $\alpha'/R_{BH}^2 = T^{3/5}$ where α' is the string coupling and R_{BH} the black hole radius. That is, generically

$$E_0 = A_0 T^{14/5} + A_1 T^{17/5} + A_2 T^{20/5} + A_3 T^{23/5} + A_4 T^{26/5} + A_5 T^{29/5} + \dots \quad (5.2)$$

However, the coefficients $A_{1,2,4}$ are known to vanish based on string theory calculations.

We tried a variety of strategies to verify from our data that those coefficients do indeed vanish. We performed a 6-parameter fit to our 7 data points, tried fixing A_0 to

³A fit of this form including a_3 reproduces a compatible value for a_1 but fails to reproduce a_2 . We find that $a_2 + a_3$ for this fit is compatible with the central value $a_2 = 5.8$ of our previous fit. This is not surprising because the corresponding powers $T^{29/5}$ and $T^{32/5}$ are very close.

its known value, tried fixing A_0 , A_3 and A_5 to the best-fit values of Sec. 5.1. In no case did we get a reliable fit, nor could we empirically confirm that these coefficients vanish. This is unsurprising, because to distinguish the terms we need to sample temperatures where, for example, $T^{14/5}$ and $T^{17/5}$ differ notably—which is difficult in the temperature range of our data. Indeed, we are fortunate that those terms vanish, because it is much easier to distinguish the different nonvanishing powers (as we did at the beginning of this section) when those powers are more widely separated. Obtaining information at smaller temperatures becomes crucial in order to determine higher order corrections more precisely.

5.2 Subleading Temperature Dependence

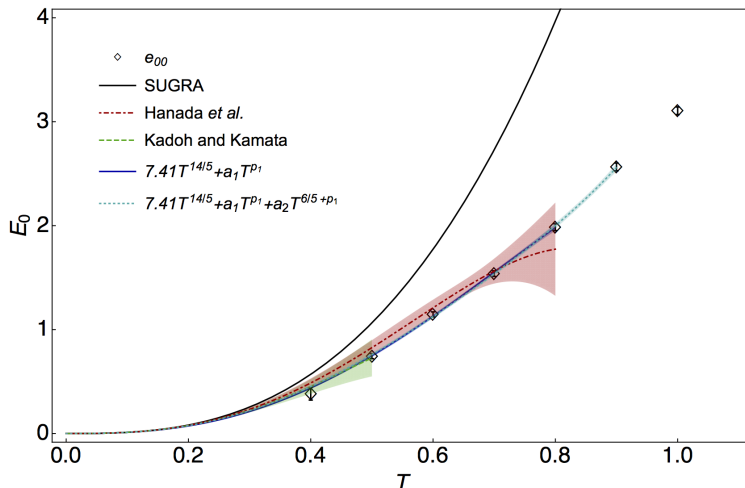


Figure 10. Two fits of our continuum large- N values e_{00} (black diamonds) for $E_0(T)$. The solid blue line is a fit to (5.3) over $0.4 \leq T \leq 0.8$, while the dotted cyan line is a fit to (5.4) over $0.4 \leq T \leq 0.9$, with their respective (small) error bands. We also show the results from Hanada et al. [30] and Kadoh and Kamata [12] as red dot-dashed and green dashed lines, respectively, with their 1σ uncertainty band as explained in the main text. The SUGRA result is shown in black.

Previous work has fit the form

$$E_0(T) = 7.41T^{14/5} + a_1T^{p_1} \quad (5.3)$$

where the exponent of the first correction is also unconstrained, but with a fixed leading behavior. Our best fit to this form is for $0.4 \leq T \leq 0.8$, yielding $a_1 = -4.7 \pm 0.2$ and $p_1 = 3.9 \pm 0.1$ ($\chi^2/\text{DOF}=1.6/3$). We are unable to reproduce the known power $p_1 = 23/5 = 4.6$ from this fit, indicating that the temperatures used in the fit were too high to identify this dependence alone, or the temperature range is too wide for the data to be described by simply the next-to-leading-order power of T .⁴ In fact, trying to incorporate the next nonzero α' correction by fitting

$$E_0(T) = 7.41T^{14/5} + a_1T^{p_1} + a_2T^{p_1+6/5} \quad (5.4)$$

⁴It is interesting to note that, if we fit our data by a single power law $E_0(T) = aT^p$, then $E_0(T) = (3.13 \pm 0.03)T^{2.02 \pm 0.03} \approx \pi T^2$ describes our continuum large- N data very well ($\chi^2/\text{DOF}=7.7/5$) in the whole temperature range. We emphasize that this may be a coincidence.

produces

$$p_1 = 4.6 \pm 0.3 \quad a_1 = -10.2 \pm 2.4 \quad a_2 = 6.2 \pm 2.6 \quad \chi^2/\text{DOF} = 2.6/3.$$

These values for a_1 and a_2 match very well with the results of the previous section, where all the powers were fixed, and p_1 matches the predicted value exactly. This fit takes advantage of the knowledge that on the gravity side the energy can be characterized by a power series in $T^{3/5}$ as explained in (5.2) and that some of the coefficients vanish.

To avoid incorporating knowledge from the string theory side, we would prefer to fit the different powers independently rather than requiring them to differ by $6/5$. However, executing such a fit is extremely tricky without imposing the qualitative requirement that the two exponents differ nontrivially. This requires a more sophisticated analysis.

In a calculation with the momentum cutoff regularization [18] at $N \leq 17$, Ref. [11] obtained $a_1 = -5.55(7)$ and $p_1 = 4.58(3)$ by using data points at $0.5 \leq T \leq 0.7$, without an explicit estimate of the discretization errors the effect of N finite. More recently, the continuum limit at $N = 16$ has been studied in Ref. [30] and we use those continuum, fixed- N results to perform an additional fit to (5.3) which is reported as ‘‘Hanada et al.’’ in Fig. 10. The resulting parameters are consistent with the ones at fixed cutoff [11], and the function $E_0(T)$ overlap with all our data points due to the large uncertainty of the fit. However, with our lattice data extrapolated to the continuum and large- N limit we have demonstrated that the next-to-leading order temperature dependence can not be singled out with accuracy, without accounting for the next α' correction.

In another lattice study described in Ref. [12], the authors obtain $a_1 = -9 \pm 2$ and $p_1 = 4.74 \pm 0.35$ from data at $0.375 \leq T \leq 0.475$, again without a continuum limit or an extrapolation to large N . In Fig. 10 we show how their results compare with our data points and the other fits in the literature. In the same range of temperatures we only have one continuum value for e_{00} which hinders our ability to reproduce their result from (5.3).⁵

5.3 $\mathcal{O}(N^{-2})$ Corrections

Because our 2D fits naturally yield e_{10} , the continuum N^{-2} contribution to E/N^2 at each temperature, we can extract the NLO N dependence in (5.1). In other words, getting values of e_{10} allows us to fit $E_1(T)$ in (5.1).

We attempted four fits of the parameters b_0 (known exactly from string theory, and approximately -5.77) and b_1 : a fit of b_0 only, a fit of b_1 fixing b_0 to its known value, and a simultaneous fit of both parameters, as well as a fit to a generic power law $b_0 T^p$. Because our data point at $T = 0.4$ has not been determined with high accuracy, we do not include it in the fits. All fit forms do a good job describing our data, due to the large uncertainties in the values of e_{10} , and can be seen in Fig. 11.

We observe general consistency with the known values, but cannot confidently extract precision values. The two-parameter fit yields $b_0 = -5.8 \pm 3.0$ —the central value reproducing the known value, but with $\sim 50\%$ uncertainty—and a very large uncertainty on $b_1 = -3.4 \pm 5.7$. However, the central value of b_1 for that fit is concordant with central

⁵In Figure 10 the uncertainty band for the fit to the data points in Ref. [30] is obtained by actually performing the fit to the published data, while we rely on a private communication with the authors of Ref. [12] for the uncertainty band in that case.

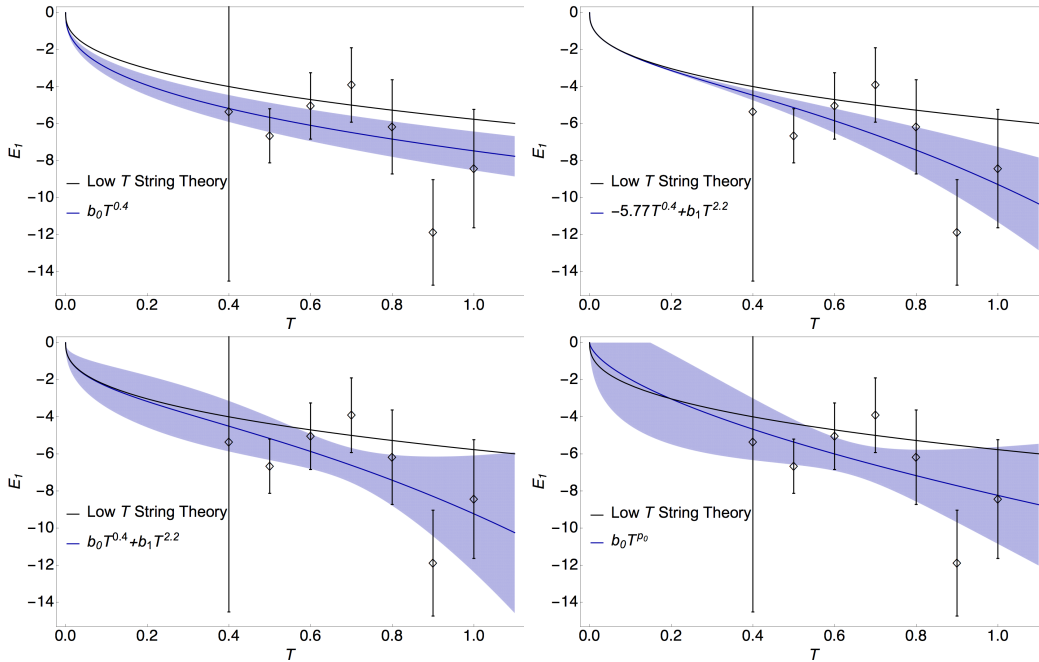


Figure 11. Four fits of E_1 to our values for e_{10} . In each panel, we show our measurements as black diamonds with 1σ error bars, the fit as the solid blue curve with a 1σ error band, and the known low-temperature behavior $b_0 = -5.77$ as the black curve. In the top left panel we fit just b_0 , with $b_1 = 0$. In the top right panel we fix $b_0 = -5.77$ and fit b_1 . In the bottom left panel we fit both b_0 and b_1 . In the bottom right panel we fit $b_0 T^{p_0}$. All fits have $0.9 < \chi^2/\text{DOF} < 1.3$, and cannot be meaningfully distinguished by our data due to the large uncertainties.

value of the fit with fixed b_0 , -3.5 ± 2.0 , which may give a modicum of confidence to the two-parameter fit.

Smaller uncertainties on the data points and lower temperatures are required to perform precision comparisons between the gravity and gauge theory at $\mathcal{O}(N^{-2})$. One strategy might be to calculate at smaller N to enhance the correction terms, but, unfortunately, it is difficult to probe small N because the Monte Carlo simulations find flat directions more quickly. This clearly hinders our ability to observe effects beyond $\mathcal{O}(N^{-2})$.⁶

6 Discussion

We have started a systematic, large-scale lattice simulation of the D0-brane quantum mechanics. In particular, we have performed the extrapolation of the internal energy to the continuum limit and to large N in a wide range of temperatures. This enabled us to do a precision test of the gauge/gravity duality. By assuming the form of the temperature dependence coming from supergravity calculations

$$\frac{E}{N^2} = \frac{(a_0 T^{14/5} + a_1 T^{23/5} + a_2 T^{29/5} + a_3 T^{32/5} \dots)}{N^0} + \frac{(b_0 T^{2/5} + b_1 T^{11/5} + \dots)}{N^2} + \mathcal{O}\left(\frac{1}{N^4}\right) \quad (6.1)$$

⁶Note however that a method introduced and used in Ref. [20] might help in the current parameter region.

we can check the agreement between supergravity and the D0-brane quantum mechanics, where results for the latter come from lattice Monte Carlo simulations. The fit results are summarized in Tab. 2.

	free	a_0 fixed		free	b_0 fixed
a_0	7.4 ± 0.5	7.41	b_0	-5.8 ± 3.0	-5.77
a_1	-9.7 ± 2.2	-10.0 ± 0.4	b_1	-3.4 ± 5.7	-3.5 ± 2.0
a_2	5.6 ± 1.8	5.8 ± 0.5			

Table 2. A summary of our fit results for E/N^2 parametrized as in Equation 6.1, using only knowledge of the powers of the temperature dependence. These results are described in greater detail in Sections 5.1, 5.2, and 5.3. The two columns for each quantity are the results from the totally free fit and the fit where the leading behavior is fixed to the known value.

For the first time we have directly determined the leading coefficient a_0 and obtained $a_0 = 7.4 \pm 0.5$, which nicely agrees with 7.41, the value known from the supergravity calculation. We also determined the next-to-leading temperature dependence $a_1 = -10.2 \pm 2.4$ and $p_1 = 4.6 \pm 0.3$ in the continuum limit, and found agreement with Ref. [12].

The precision of our large- N , continuum extrapolated points makes it hard to believe that dramatic improvements can be achieved through larger statistical sampling. Instead, to reduce our $\sim 7\%$ error on a_0 we would require more data points or simulations at lower temperatures. Unfortunately, stabilizing the Monte Carlo simulations at lower temperatures requires going to even larger values of N which is numerically costly. For the same reason it is challenging to obtain a precise determination of $E_1(T)$, the $1/N^2$ corrections, in the parameter region we considered, where we had to use $N \geq 16$. However, we were able to extract general agreement with the known $b_0 = -5.77$, albeit with sizable uncertainty.

We believe that the current results demonstrate the power of large-scale supercomputer simulations applied to superstring theory. A number of future directions are definitely worth investigating. Besides increasing the precision of the numerical results presented in our study to test the duality between the D0-brane quantum mechanics and type IIA superstring even more accurately, we will focus on the very low temperature region where the system is expected to be described by M-theory [4–6]. Studying super Yang-Mills in other spacetime dimensions with an equally large-scale study is another important direction.

While testing the duality is crucial, framing quantum gravitational puzzles in terms of the gauge theory could be especially rewarding. Can one see the emergence of the bulk spacetime from the gauge theory? Is there a firewall? Is it possible to explicitly trace the unitary evaporation of the black hole? Fascinating frontiers lie ahead.

Acknowledgements

M. H. would like to thank Y. Hyakutake for discussions. The work of M. H. is supported in part by the Grant-in-Aid of the Japanese Ministry of Education, Sciences and Technology, Sports and Culture (MEXT) for Scientific Research (No. 25287046). The work of G. I. was

supported, in part, by Program to Disseminate Tenure Tracking System, MEXT, Japan and by KAKENHI (16K17679). S. S. was supported by the MEXT-Supported Program for the Strategic Research Foundation at Private Universities “Topological Science” (Grant No. S1511006) This work was performed under the auspices of the U.S. Department of Energy by Lawrence Livermore National Laboratory under contract DE-AC52-07NA27344. Numerical calculations were performed on the Vulcan BlueGene/Q at LLNL, supported by the LLNL Multiprogrammatic and Institutional Computing program through a Tier 1 Grand Challenge award and on the RIKEN K Computer.

References

- [1] Juan Martin Maldacena. The Large N limit of superconformal field theories and supergravity. *Int. J. Theor. Phys.*, 38:1113–1133, 1999. [Adv. Theor. Math. Phys.2,231(1998)].
- [2] S. S. Gubser, Igor R. Klebanov, and Alexander M. Polyakov. Gauge theory correlators from noncritical string theory. *Phys. Lett.*, B428:105–114, 1998.
- [3] Edward Witten. Anti-de Sitter space and holography. *Adv. Theor. Math. Phys.*, 2:253–291, 1998.
- [4] Nissan Itzhaki, Juan Martin Maldacena, Jacob Sonnenschein, and Shimon Yankielowicz. Supergravity and the large N limit of theories with sixteen supercharges. *Phys. Rev.*, D58:046004, 1998.
- [5] Tom Banks, W. Fischler, S. H. Shenker, and Leonard Susskind. M theory as a matrix model: A Conjecture. *Phys. Rev.*, D55:5112–5128, 1997.
- [6] Bernard De Wit, Jens Hoppe, and Hermann Nicolai. On the quantum mechanics of supermembranes. *Nuclear Physics B*, 305(4):545–581, 1988.
- [7] Edward Witten. Bound states of strings and p-branes. *Nucl. Phys.*, B460:335–350, 1996.
- [8] Evan Berkowitz, Masanori Hanada, and Jonathan Maltz. A Microscopic Description of Black Hole Evaporation via Holography. 2016.
- [9] Konstantinos N. Anagnostopoulos, Masanori Hanada, Jun Nishimura, and Shingo Takeuchi. Monte Carlo studies of supersymmetric matrix quantum mechanics with sixteen supercharges at finite temperature. *Phys. Rev. Lett.*, 100:021601, 2008.
- [10] Daniel N. Kabat, Gilad Lifschytz, and David A. Lowe. Black hole thermodynamics from calculations in strongly coupled gauge theory. *Int. J. Mod. Phys.*, A16:856–865, 2001. [,216(2000)].
- [11] Masanori Hanada, Yoshifumi Hyakutake, Jun Nishimura, and Shingo Takeuchi. Higher derivative corrections to black hole thermodynamics from supersymmetric matrix quantum mechanics. *Phys. Rev. Lett.*, 102:191602, 2009.
- [12] Daisuke Kadoh and Syo Kamata. Gauge/gravity duality and lattice simulations of one dimensional SYM with sixteen supercharges. 2015.
- [13] Simon Catterall and Toby Wiseman. Black hole thermodynamics from simulations of lattice Yang-Mills theory. *Phys. Rev.*, D78:041502, 2008.
- [14] Veselin G. Filev and Denjoe O’Connor. The BFSS model on the lattice. 2015.
- [15] Masanori Hanada, Akitsugu Miwa, Jun Nishimura, and Shingo Takeuchi. Schwarzschild radius from Monte Carlo calculation of the Wilson loop in supersymmetric matrix quantum mechanics. *Phys. Rev. Lett.*, 102:181602, 2009.

- [16] Masanori Hanada, Jun Nishimura, Yasuhiro Sekino, and Tamiaki Yoneya. Monte Carlo studies of Matrix theory correlation functions. Phys. Rev. Lett., 104:151601, 2010.
- [17] Masanori Hanada, Jun Nishimura, Yasuhiro Sekino, and Tamiaki Yoneya. Direct test of the gauge-gravity correspondence for Matrix theory correlation functions. JHEP, 12:020, 2011.
- [18] Masanori Hanada, Jun Nishimura, and Shingo Takeuchi. Non-lattice simulation for supersymmetric gauge theories in one dimension. Phys. Rev. Lett., 99:161602, 2007.
- [19] M. Hanada. <https://sites.google.com/site/hanadamasanori/home/mmmm>, 2016.
- [20] Masanori Hanada, Yoshifumi Hyakutake, Goro Ishiki, and Jun Nishimura. Holographic description of a quantum black hole on a computer. Science, 344(6186):882–885, 2014.
- [21] Masanori Hanada and Issaku Kanamori. Absence of sign problem in two-dimensional $N = (2,2)$ super Yang-Mills on lattice. JHEP, 01:058, 2011.
- [22] David J. Gross and Edward Witten. Superstring Modifications of Einstein’s Equations. Nucl. Phys., B277:1, 1986.
- [23] David J. Gross and John H. Sloan. The Quartic Effective Action for the Heterotic String. Nucl. Phys., B291:41–89, 1987.
- [24] Marcus T. Grisaru, A. E. M. van de Ven, and D. Zanon. Four Loop beta Function for the $N=1$ and $N=2$ Supersymmetric Nonlinear Sigma Model in Two-Dimensions. Phys. Lett., B173:423–428, 1986.
- [25] Marcus T. Grisaru and D. Zanon. σ Model Superstring Corrections to the Einstein-hilbert Action. Phys. Lett., B177:347–351, 1986.
- [26] Michael B. Green and Pierre Vanhove. The Low-energy expansion of the one loop type II superstring amplitude. Phys. Rev., D61:104011, 2000.
- [27] Michael B. Green, Jorge G. Russo, and Pierre Vanhove. Non-renormalisation conditions in type II string theory and maximal supergravity. JHEP, 02:099, 2007.
- [28] Yoshifumi Hyakutake. Quantum near-horizon geometry of a black 0-brane. PTEP, 2014:033B04, 2014.
- [29] Yoshifumi Hyakutake. Quantum M-wave and Black 0-brane. JHEP, 09:075, 2014.
- [30] Masanori Hanada, Yoshifumi Hyakutake, Goro Ishiki, and Jun Nishimura. Numerical tests of the gauge/gravity duality conjecture for D0-branes at finite temperature and finite N . 2016.

A Correlations Between Polyakov Loop and Internal Energy

In this section we analyze the possible presence of correlations in the distributions of the Polyakov loop $|P|$ (cfr. (3.12)) and of the internal energy E/N^2 (cfr. (3.11)). Our aim is to test how similar the distributions of $|P|$ are for different values of E/N^2 . To compare distributions of samples drawn in the same Monte Carlo simulation, it is useful to apply the two-sample Kolmogorov-Smirnov (KS) test. This test is designed to give a statistical measure to the similarity of two distributions.

In practice, given two data sets of size n_1 and n_2 with their corresponding empirical distribution functions $F_{n_1}^{(1)}(x)$ and $F_{n_2}^{(2)}(x)$, the KS statistic is

$$D(n_1, n_2) \equiv D = \sup_x |F_{n_1}^{(1)}(x) - F_{n_2}^{(2)}(x)| . \quad (\text{A.1})$$

This statistic tests the hypothesis that the distributions of the two data sets are the same. If $D(n_1, n_2)$ is larger than a critical value, the distributions are not the same with an associated confidence level. Often the confidence level is expressed in terms of a p-value.⁷ We use the KS test and reject the hypothesis that two $|P|$ distributions are the same if the associated p-value is less than 1%.

We compare two distributions that have the same number of samples— for example $1/12 \sim 8\%$ of the whole set. Therefore, we start from our Monte Carlo history of E/N^2 and select 8% of the configurations with the smallest energy. Then we select the next 8% and so on. For each 8% bin of configurations, we look at the distribution of the Polyakov loop and compare them pair-wise. We also repeat this analysis with bins containing only 4% of the configurations each, noticing no significant differences.

For example, in the case of our $N = 16$, $L = 16$ and $T = 0.8$ ensemble we find out that the test is successful $> 92\%$ of the time. Two distributions passing the test are shown in Fig. 12. We also notice that the failing tests occur for energy intervals near the tail of the energy distribution. In such cases it is clearly harder to obtain a faithful sampling of the distribution. Moreover, an equivalence of the Polyakov loop distributions in the tail of the energy fluctuations is not strictly required to corroborate our argument in Section 3.3 about the validity of the phase-quenched approximation of the Pfaffian. An example of the KS test in the tail of the energy distribution is shown in Fig. 13.

⁷The p-value is a well-known tool used in frequentist statistics. It is the probability of finding the observed, or more extreme, results when the hypothesis is true. Large p-values support the hypothesis.

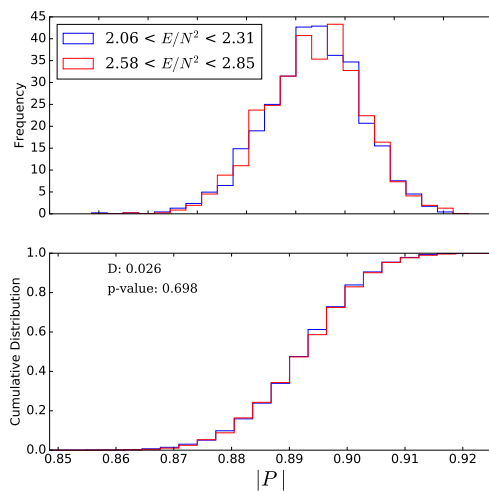


Figure 12. The distributions of $|P|$ at $N = 16$, $L = 16$ and $T = 0.8$ for different energy intervals reported in the legend. These energy intervals are close to the average value of E/N^2 for this ensemble. The upper panel shows the normalized probability distribution, while the lower panel shows the cumulative distribution as a proxy for the empirical distribution function used in the KS test. The value of the KS statistic D and its associated p-value are also shown, giving confidence that the two underlying distributions are the same.

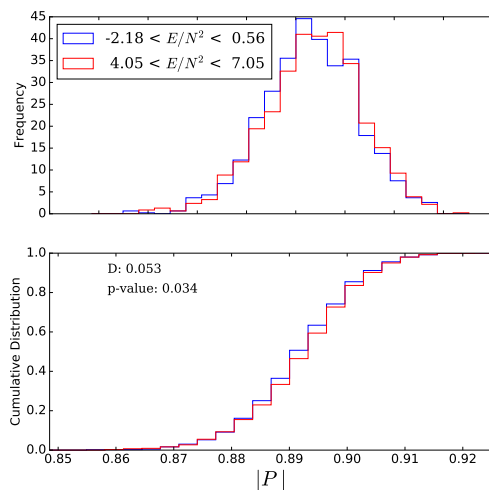


Figure 13. Same as Figure 12, but for energy intervals at the tail of the energy distribution, instead of around the average. The KS statistic is larger and the p-value is considerably lower.

B Lattice Measurements

Here we present a summary of our ensembles and corresponding measured observables.

T	N	L	action	N_{cfg}	E/N^2	$ P $	R^2	F^2	
0.4	24	16	improved	15935	0.827 ± 0.005	0.72770 ± 0.00035	3.2504 ± 0.0015	14.530 ± 0.002	
		24	improved	2321	0.719 ± 0.031	0.72888 ± 0.00129	3.3459 ± 0.0039	15.627 ± 0.011	
		32	improved	6625	0.657 ± 0.027	0.72721 ± 0.00116	3.4110 ± 0.0020	16.319 ± 0.008	
	32	8	improved	3057	0.903 ± 0.009	0.74150 ± 0.00348	4.8789 ± 0.0967	13.846 ± 0.006	
		12	improved	2491	0.907 ± 0.010	0.72754 ± 0.00089	3.1663 ± 0.0024	13.651 ± 0.005	
		16	improved	8242	0.835 ± 0.007	0.72732 ± 0.00054	3.2387 ± 0.0012	14.518 ± 0.003	
		24	improved	1331	0.692 ± 0.052	0.72919 ± 0.00453	3.3414 ± 0.0025	15.635 ± 0.012	
		32	improved	1888	0.629 ± 0.029	0.72849 ± 0.00142	3.4016 ± 0.0018	16.311 ± 0.008	
0.5	16	8	improved	21101	1.229 ± 0.004	0.78847 ± 0.00031	3.1104 ± 0.0026	13.068 ± 0.003	
		12	improved	17201	1.140 ± 0.007	0.79566 ± 0.00032	3.2304 ± 0.0014	14.374 ± 0.003	
		16	improved	17933	1.081 ± 0.009	0.79599 ± 0.00035	3.3086 ± 0.0012	15.207 ± 0.004	
		32	improved	15101	0.907 ± 0.020	0.79689 ± 0.00049	3.4747 ± 0.0017	16.897 ± 0.006	
	24	8	improved	20951	1.243 ± 0.004	0.78964 ± 0.00028	3.0776 ± 0.0007	13.038 ± 0.002	
		16	improved	19765	1.092 ± 0.006	0.79718 ± 0.00020	3.2883 ± 0.0005	15.194 ± 0.002	
		24	improved	14957	0.979 ± 0.010	0.79741 ± 0.00029	3.3898 ± 0.0006	16.240 ± 0.003	
		32	improved	10469	0.941 ± 0.024	0.79727 ± 0.00051	3.4457 ± 0.0012	16.851 ± 0.007	
		32	8	improved	16253	1.248 ± 0.003	0.78995 ± 0.00020	3.0712 ± 0.0006	13.032 ± 0.002
			12	improved	3569	1.155 ± 0.010	0.79600 ± 0.00049	3.2012 ± 0.0010	14.357 ± 0.004
	16		improved	7885	1.093 ± 0.009	0.79730 ± 0.00034	3.2830 ± 0.0007	15.196 ± 0.003	
	24		improved	2873	0.946 ± 0.047	0.79852 ± 0.00123	3.3815 ± 0.0032	16.223 ± 0.012	
	0.6	16	8	improved	27221	1.560 ± 0.005	0.83423 ± 0.00018	3.1410 ± 0.0006	13.728 ± 0.002
			12	improved	19051	1.475 ± 0.007	0.84077 ± 0.00021	3.2708 ± 0.0008	15.001 ± 0.003
16			improved	18141	1.432 ± 0.010	0.84156 ± 0.00023	3.3477 ± 0.0010	15.790 ± 0.004	
24			improved	8977	1.339 ± 0.021	0.84184 ± 0.00034	3.4410 ± 0.0020	16.754 ± 0.008	

T	N	L	action	N_{cfg}	E/N^2	$ P $	R^2	F^2	
0.6	16	32	improved	18677	1.267 ± 0.021	0.84181 ± 0.00028	3.4951 ± 0.0014	17.327 ± 0.006	
		24	8	improved	23971	1.569 ± 0.004	0.83474 ± 0.00017	3.1290 ± 0.0005	13.731 ± 0.002
			12	improved	19171	1.481 ± 0.007	0.84083 ± 0.00018	3.2602 ± 0.0007	15.012 ± 0.003
			16	improved	19961	1.429 ± 0.008	0.84205 ± 0.00018	3.3349 ± 0.0006	15.790 ± 0.003
			24	improved	25249	1.346 ± 0.009	0.84176 ± 0.00015	3.4262 ± 0.0006	16.753 ± 0.003
			32	improved	12577	1.276 ± 0.025	0.84212 ± 0.00030	3.4780 ± 0.0012	17.309 ± 0.007
		32	8	improved	19017	1.575 ± 0.005	0.83539 ± 0.00024	3.1248 ± 0.0007	13.731 ± 0.003
			16	improved	10071	1.442 ± 0.009	0.84182 ± 0.00022	3.3306 ± 0.0006	15.787 ± 0.004
0.7	16	8	improved	30641	1.959 ± 0.005	0.86564 ± 0.00013	3.1941 ± 0.0006	14.377 ± 0.003	
			12	improved	20051	1.885 ± 0.008	0.87096 ± 0.00014	3.3145 ± 0.0008	15.579 ± 0.004
			16	improved	20187	1.843 ± 0.011	0.87181 ± 0.00015	3.3891 ± 0.0009	16.333 ± 0.005
			24	improved	10605	1.763 ± 0.022	0.87126 ± 0.00024	3.4702 ± 0.0018	17.214 ± 0.009
			32	unimproved	21633	2.344 ± 0.031	0.86981 ± 0.00017	3.5681 ± 0.0015	18.615 ± 0.007
				improved	19921	1.672 ± 0.023	0.87191 ± 0.00021	3.5193 ± 0.0014	17.739 ± 0.007
		24	8	improved	20701	1.968 ± 0.005	0.86574 ± 0.00014	3.1854 ± 0.0005	14.385 ± 0.003
			12	improved	19997	1.893 ± 0.008	0.87095 ± 0.00013	3.3088 ± 0.0007	15.601 ± 0.004
			16	improved	21451	1.849 ± 0.007	0.87203 ± 0.00012	3.3789 ± 0.0006	16.338 ± 0.004
			24	improved	28925	1.755 ± 0.011	0.87126 ± 0.00012	3.4634 ± 0.0007	17.237 ± 0.004
			32	improved	16135	1.682 ± 0.025	0.87186 ± 0.00019	3.5069 ± 0.0012	17.726 ± 0.008
		32	8	improved	18989	1.966 ± 0.006	0.86612 ± 0.00017	3.1837 ± 0.0007	14.394 ± 0.004
			16	improved	10849	1.850 ± 0.010	0.87187 ± 0.00015	3.3771 ± 0.0008	16.341 ± 0.004
	0.8	16	8	unimproved	19281	3.674 ± 0.009	0.89048 ± 0.00013	3.5758 ± 0.0028	17.845 ± 0.008
			improved	19171	2.400 ± 0.008	0.88790 ± 0.00012	3.2468 ± 0.0007	14.994 ± 0.004	
		12	improved	22001	2.356 ± 0.009	0.89220 ± 0.00011	3.3601 ± 0.0008	16.138 ± 0.005	
		16	unimproved	24081	3.283 ± 0.016	0.89113 ± 0.00011	3.5305 ± 0.0011	18.305 ± 0.006	
			improved	21421	2.309 ± 0.012	0.89318 ± 0.00011	3.4295 ± 0.0010	16.856 ± 0.005	
		24	unimproved	21591	3.000 ± 0.025	0.89069 ± 0.00012	3.5588 ± 0.0012	18.663 ± 0.007	
			improved	17521	2.214 ± 0.019	0.89292 ± 0.00014	3.5070 ± 0.0013	17.687 ± 0.008	
		32	unimproved	14157	2.710 ± 0.044	0.89119 ± 0.00017	3.5803 ± 0.0016	18.880 ± 0.010	

T	N	L	action	N_{cfg}	E/N^2	$ P $	R^2	F^2	
0.8	16	32	improved	20187	2.107 ± 0.024	0.89261 ± 0.00015	3.5452 ± 0.0014	18.131 ± 0.009	
		24	8	improved	22151	2.417 ± 0.006	0.88779 ± 0.00011	3.2416 ± 0.0006	15.010 ± 0.003
			12	improved	18175	2.346 ± 0.009	0.89207 ± 0.00011	3.3553 ± 0.0008	16.155 ± 0.005
			16	improved	20721	2.303 ± 0.010	0.89317 ± 0.00009	3.4232 ± 0.0007	16.868 ± 0.004
			24	improved	9153	2.216 ± 0.020	0.89239 ± 0.00015	3.4968 ± 0.0012	17.681 ± 0.008
			32	improved	13867	2.176 ± 0.028	0.89287 ± 0.00015	3.5366 ± 0.0015	18.134 ± 0.009
		32	8	improved	19213	2.424 ± 0.007	0.88809 ± 0.00014	3.2394 ± 0.0008	15.012 ± 0.004
			16	improved	13495	2.340 ± 0.017	0.89302 ± 0.00018	3.4216 ± 0.0014	16.869 ± 0.008
	0.9	16	8	unimproved	20411	4.221 ± 0.010	0.90519 ± 0.00009	3.5113 ± 0.0012	17.926 ± 0.005
				improved	20401	2.895 ± 0.009	0.90433 ± 0.00009	3.3002 ± 0.0008	15.599 ± 0.004
			12	improved	20501	2.863 ± 0.011	0.90783 ± 0.00009	3.4048 ± 0.0009	16.679 ± 0.005
			16	unimproved	37701	3.710 ± 0.014	0.90689 ± 0.00007	3.5475 ± 0.0007	18.635 ± 0.005
				improved	21461	2.796 ± 0.014	0.90856 ± 0.00009	3.4717 ± 0.0010	17.377 ± 0.006
			24	unimproved	21851	3.450 ± 0.028	0.90639 ± 0.00010	3.5807 ± 0.0013	19.001 ± 0.008
				improved	17955	2.716 ± 0.021	0.90826 ± 0.00011	3.5400 ± 0.0014	18.139 ± 0.009
			32	unimproved	12221	3.243 ± 0.049	0.90720 ± 0.00013	3.6037 ± 0.0019	19.209 ± 0.012
				improved	14601	2.673 ± 0.031	0.90849 ± 0.00013	3.5750 ± 0.0017	18.545 ± 0.011
		24	8	improved	24331	2.931 ± 0.006	0.90413 ± 0.00008	3.2958 ± 0.0006	15.613 ± 0.004
			12	improved	17557	2.872 ± 0.010	0.90785 ± 0.00009	3.4025 ± 0.0009	16.707 ± 0.006
			16	improved	24441	2.822 ± 0.010	0.90861 ± 0.00007	3.4658 ± 0.0007	17.384 ± 0.005
			24	improved	8917	2.761 ± 0.023	0.90774 ± 0.00013	3.5349 ± 0.0014	18.156 ± 0.009
			32	improved	16709	2.719 ± 0.028	0.90824 ± 0.00010	3.5663 ± 0.0014	18.538 ± 0.009
		32	8	improved	18695	2.931 ± 0.008	0.90441 ± 0.00011	3.2948 ± 0.0009	15.620 ± 0.005
			16	improved	12061	2.835 ± 0.019	0.90836 ± 0.00016	3.4643 ± 0.0016	17.388 ± 0.009
1.0		16	8	unimproved	21291	4.719 ± 0.011	0.91705 ± 0.00007	3.5139 ± 0.0010	18.245 ± 0.006
				improved	20641	3.439 ± 0.010	0.91672 ± 0.00008	3.3515 ± 0.0009	16.185 ± 0.005
			12	improved	20751	3.397 ± 0.012	0.91968 ± 0.00008	3.4485 ± 0.0010	17.217 ± 0.006
				unimproved	25379	4.185 ± 0.019	0.91907 ± 0.00007	3.5769 ± 0.0010	19.034 ± 0.007
			16	improved	21641	3.378 ± 0.015	0.92033 ± 0.00008	3.5115 ± 0.0011	17.876 ± 0.007

T	N	L	action	N_{cfg}	E/N^2	$ P $	R^2	F^2
1.0	16	24	unimproved	23391	3.937 ± 0.030	0.91855 ± 0.00008	3.6099 ± 0.0013	19.376 ± 0.009
			improved	17469	3.290 ± 0.024	0.91979 ± 0.00009	3.5755 ± 0.0017	18.600 ± 0.011
		32	unimproved	13503	3.690 ± 0.054	0.91895 ± 0.00012	3.6323 ± 0.0019	19.582 ± 0.013
			improved	15555	3.185 ± 0.034	0.91985 ± 0.00011	3.6068 ± 0.0018	18.971 ± 0.013
		48	unimproved	12026	3.534 ± 0.092	0.92064 ± 0.00014	3.6592 ± 0.0028	19.810 ± 0.021
			improved	5772	3.154 ± 0.094	0.92101 ± 0.00025	3.6431 ± 0.0042	19.401 ± 0.027
		64	unimproved	15024	3.505 ± 0.112	0.92051 ± 0.00015	3.6808 ± 0.0029	19.999 ± 0.020
			improved	7280	3.210 ± 0.105	0.92070 ± 0.00021	3.6752 ± 0.0042	19.715 ± 0.030
	24	8	improved	22605	3.467 ± 0.007	0.91663 ± 0.00007	3.3490 ± 0.0007	16.208 ± 0.004
			improved	19817	3.413 ± 0.011	0.91956 ± 0.00007	3.4478 ± 0.0009	17.251 ± 0.006
			improved	20655	3.363 ± 0.013	0.92041 ± 0.00007	3.5084 ± 0.0009	17.901 ± 0.006
			improved	21725	3.283 ± 0.019	0.91964 ± 0.00008	3.5705 ± 0.0011	18.609 ± 0.008
			improved	19383	3.268 ± 0.028	0.91997 ± 0.00009	3.5993 ± 0.0014	18.964 ± 0.010
			improved	17881	3.469 ± 0.008	0.91684 ± 0.00009	3.3482 ± 0.0009	16.216 ± 0.006
	32	16	improved	14915	3.386 ± 0.019	0.92018 ± 0.00011	3.5078 ± 0.0013	17.902 ± 0.009

C Simultaneous Continuum Large- N Extrapolations

Here we give a more complete version Table 1, summarizing our simultaneous extrapolation to the continuum, large- N limit via (4.3), including the lattice-spacing effects and all the off-diagonal entries of the covariance matrix.

T	e_{00}	$-e_{10}$	e_{01}	$-e_{02}$	$\Sigma_{00,10}$	$\Sigma_{00,01}$	$\Sigma_{00,02}$	$\Sigma_{10,01}$	$\Sigma_{10,02}$	$\Sigma_{01,02}$	χ^2	DOF
0.4	0.38±0.06	5.4±9.2	10.0±1.8	44±15	-0.1631	-0.11	0.79	-0.36	15.9	-28	1.3	4
0.5	0.74±0.02	6.7±1.5	7.2±0.6	25±3	+0.0005	-0.01	0.08	-0.14	0.8	-2	7.2	9
0.6	1.15±0.02	5.0±1.8	5.8±0.6	19±3	-0.0046	-0.01	0.08	-0.07	0.4	-2	8.8	8
0.7	1.54±0.03	3.9±2.0	6.4±0.7	23±3	-0.0066	-0.02	0.09	-0.07	0.4	-2	8.8	8
0.8	1.99±0.03	6.2±2.5	7.0±0.8	28±4	-0.0151	-0.02	0.13	-0.09	0.8	-3	15.1	8
0.9	2.57±0.04	11.9±2.9	5.9±0.9	23±4	-0.0192	-0.03	0.17	-0.08	0.8	-4	3.3	8
1.0	3.11±0.04	8.4±3.2	5.9±0.9	23±4	-0.0218	-0.03	0.16	-0.15	1.3	-4	8.9	10

If measurements of variables x_i are normally distributed, then naïvely their joint probability distribution P might be

$$P(x) = c e^{-\frac{1}{2} \sum_i \left(\frac{x_i - \mu_i}{\sigma_i} \right)^2} \quad (\text{C.1})$$

where μ_i represents the central value and σ_i the spread in the measurement of (ie. the uncertainty of) variable x_i , and c is a normalization constant. However, more generically the measurements might be distributed according to

$$P(x) = c e^{-\frac{1}{2} (x - \mu)_i \Sigma_{ij}^{-1} (x - \mu)_j} \quad (\text{C.2})$$

where Σ is the covariance matrix, a symmetric positive-definite matrix. The uncertainty on a single variable x_i is $\sqrt{\Sigma_{ii}}$. An off-diagonal entry in the covariance matrix indicates how the errors on the two variables i and j are correlated. We use the shorthand that the two subscripts on Σ are the subscripts on the corresponding e variables.

We determine the best fit by minimizing the usual χ^2 fit metric. We fix the covariant errors by finding the values of the variables where the minimal χ^2 increases by 1 (or, equivalently, where P decreases by $1/e$).